Engineering Fracture Mechanics 78 (2011) 901–918

Contents lists available at ScienceDirect

Engineering Fracture Mechanics

journal homepage: www.elsevier.com/locate/engfracmech

Multiscale simulation of fracture of braided composites via repetitive unit cells

Vít Šmilauer [a,1], Christian G. Hoover [a], Zdeněk P. Bažant [b,*], Ferhun C. Caner [c], Anthony M. Waas [d], Khaled W. Shahwan [e]

[a] Northwestern University, 2145 Sheridan Road, Evanston, IL 60208, USA
[b] Departments of Civil Engineering and Materials Science, Northwestern University, 2145 Sheridan Road, CEE/A135, Evanston, IL 60208, USA
[c] Institute of Energy Technologies, Technical University of Catalonia, Diagonal 647, E-08028 Barcelona, Spain
[d] Dept. of Aeronautical Engrg., University of Michigan, Ann Arbor, MI, USA
[e] Director—Board of Directors of the Automotive Composites Consortium (ACC), and Chairman of the ACC100 Group, U.S. Council for Automotive Research (USCAR), and Chrysler Group LLC, Chrysler Technology Center, Auburn Hills, MI, USA

ARTICLE INFO

Article history:
Received 4 February 2010
Received in revised form 22 October 2010
Accepted 26 October 2010
Available online 3 November 2010

Keywords:
Composites
Polymer matrix composites
Damage mechanics
Finite element analysis
Fracture mechanics
Failure
Brittle fracture
Automotive components
Crashworthiness
Energy absorption
Rail post
Rail post crushing

ABSTRACT

Two-dimensional triaxially braided composites (2DTBCs) are attractive in crashworthiness design because their fracture can dissipate a significantly larger amount of impact energy than other light-weight materials. This paper aims at predicting the fracture energy, G_f, and the effective length of the fracture process zone, c_f, of 2DTBC composites. Since the fracture parameters are best manifested in the scaling properties and are the main parameters in the size effect law, the nominal strengths of three geometrically similar notched beams of three different sizes are simulated in a 3D finite element framework. The simulations are run for three different bias tow angles: 30°, 45° and 60°. Continuum beam elements in front of the notch are replaced with repetitive unit cells (RUCs), which represent the 2DTBC's mesostructure, and are located in the region of potential cracking. Multiscale simulations, incorporating damage mechanics, are used to predict the pre- and post-peak response from three-point bending tests. Nominal stresses are calculated from the predicted peak loads and used to fit the size effect law. The dimensionless energy release rate function $g(\alpha)$ is determined from the J-integral. The values of G_f and c_f are then determined using $g(\alpha)$ and the size effect law. With some exceptions, the results in general match well with the results of size effect experiments, and particularly the strong size effect observed in the tests.

1. Introduction and objective

Two-dimensional triaxially braided composites (2DTBCs), fabricated from carbon fiber tows and bound by epoxy matrix, can exhibit high fracture energies [1]. This makes them highly desirable for energy dissipating structures. To maximize the energy dissipation, the material and geometric properties must be optimized. This task is facilitated by developing a good computational model that reduces the need for time-consuming experiments.

* Corresponding author. Tel.: +1 847 491 4025; fax: +1 847 491 4011.
E-mail addresses: vit.smilauer@fsv.cvut.cz (V. Šmilauer), c-hoover@northwestern.edu (C.G. Hoover), z-bazant@northwestern.edu (Z.P. Bažant), ferhun.caner@upc.edu (F.C. Caner), dcw@umich.edu (A.M. Waas), kws8@chrysler.com (K.W. Shahwan).
[1] On leave from Czech Technical University in Prague, Thákurova 7, 166 29 Prague, Czech Republic.

0013-7944/$ - see front matter © 2010 Elsevier Ltd. All rights reserved.
doi:10.1016/j.engfracmech.2010.10.013

Modeling of 2DTBCs by finite elements (FE) has led to progress, but challenges remain. Previous FE simulations have been performed on heterogeneous woven composites [2,3] and on 2DTBCs [4–7]. The compressive fracturing of 2DTBC tubular structures has been analyzed but without reference to the mesostructure of braided tows and polymer [8,9].

Although realistic mesostructure-based analysis of large composite structures poses excessive computational demands, for smaller structures it is feasible; cf. [10]. The multiscale methods allow, in principle, a more realistic representation of the macroscale material properties but are controversial in the case of localization of softening damage, with the associated characteristic length and size effects [12,13].

One of the first classes of multiscale models relies on the concept of a "hierarchical" scale representation and scale separation [14,15]. In these models, information derived from the simulation of a subscale is passed in the form of a constitutive law or a homogenized property back into a macroscale continuum point, typically to the integration point of a finite element. On the subscale, periodic boundary conditions are an effective common choice. They can be further enhanced with strain gradients [15].

Such an approach, in which a subscale model is embedded in a macro-continuum point, is suitable for elastic and plastic hardening behavior but is unjustified for the prediction of softening fracturing behavior purely from the subscale. The problem arises due to the fact that the damage localization and the associated material characteristic length on both the macroscale and the subscale are incompatible with the assumed boundary conditions and the characteristic length must be assumed, rather than predicted from the subscale, which defeats the purpose of the multiscale approach.

Another class of multiscale models, which has been termed as "concurrent", e.g. [16–18], leads to a simultaneous solution of an equation system, although the system can, of course, be further decomposed for multiple processing [19,20] or can contain a weak form of displacement continuity between scales enforced by Lagrange multipliers [10,18]. In the concurrent models, a macroscale region of potential softening is replaced by a system of unit cells from the subscale. These cells describe the fracturing process on the subscale in a way that automatically reproduces damage localization as it develops in interaction with the rest of the structure. The salient feature of this approach is that it implies the material characteristic length.

In this paper, we apply a variant of the "concurrent" multiscale method, which correctly predicts energy dissipation and material characteristic length purely from the mesostructure. This method is applicable to all simulations where the crack path is known *a priori*. Macroscale elements in the location where the crack will propagate are replaced with the full mesoscale representation before the computation. In the present simulations, several RUCs are embedded in front of the notch. The simulations are used to predict the peak loads, which are then used to fit and calibrate the size effect law [12]. The fracture energy G_f and the effective process zone size c_f are then determined from the J-integral and the size effect law.

In a parallel study, the present problem is analyzed by approximating the fracturing of a unit cell of the mesostructure with the microplane model [21]. The microplane approach is more effective for large scale simulations of braided composite structures, while the present approach gives a more detailed picture of the local fracturing behavior and a better identification of fracture energy from size effect tests.

2. Multiscale analysis

Fig. 1 shows three scales used in the multiscale simulation of notched beams; micro, meso and macro.

2.1. Microscale

The microscale discerns inhomogeneities below 5 mm, which include the individual carbon fibers connected by epoxy resin. The elastic properties of the axial and bias (or braider) tows are determined by the rule-of-mixtures (other models such as the concentric cylinder model at the microscale are more commonplace) as a combination of elastic constants of the fibers and epoxy matrix;

$$G_{f,m} = \frac{E_{f,m}}{2(1+\nu_{f,m})}, \tag{1}$$

$$E'_m = \frac{E_m}{1-\nu_m^2}, \tag{2}$$

$$E_{11} = V_f E_f + V_m E_m, \tag{3}$$

$$E_{22} = E_{33} = \left(\frac{V_f}{E_f} + \frac{V_m}{E'_m}\right)^{-1}, \tag{4}$$

$$\nu_{12} = \nu_{13} = V_f \nu_f + V_m \nu_m, \tag{5}$$

$$\nu_{23} = \left(\frac{V_f}{\nu_f} + \frac{V_m}{\nu_m}\right)^{-1}, \tag{6}$$

$$G_{12} = G_{13} = \left(\frac{V_f}{G_f} + \frac{V_m}{G_m}\right)^{-1}, \tag{7}$$

where subscript 11 refers to the direction aligned with the fibers.

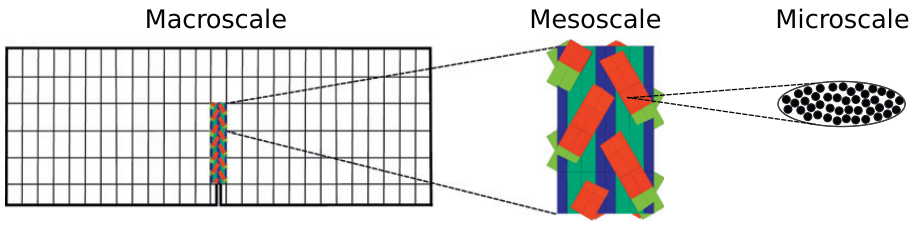

Fig. 1. Macro, meso and microscale of the problem.

Table 1
Elastic properties assigned to bias tows and epoxy matrix, the moduli are in GPa. Results computed by the rule-of-mixture.

Bias tow angle ϕ		30°	45°	60°
Carbon fiber		$E_f = 231$[a] GPa, $\nu_f = 0.14 \rightarrow G_f = 101.32$ GPa		
Epoxy resin		$E_m = 7.52$[b] GPa, $\nu_m = 0.36 \rightarrow G_m = 2.76$ GPa		
Axial tows	V_f	0.77	0.64	0.62
	E_{11}	179.6	150.3	146.1
	$E_{22} = E_{33}$	33.38	22.45	21.43
	$\nu_{12} = \nu_{13}$	0.191	0.219	0.224
	ν_{23}	0.163	0.180	0.182
	$G_{12} = G_{13}$	11.01	7.31	6.97
Bias tows	V_f	0.71	0.56	0.54
	E_{11}	165.7	132.9	128.4
	$E_{22} = E_{33}$	27.13	18.78	18.03
	$\nu_{12} = \nu_{13}$	0.204	0.237	0.241
	ν_{23}	0.170	0.191	0.195
	$G_{12} = G_{13}$	8.88	6.09	5.84

[a] According to [6].
[b] Resin modulus reported 7.52 [4] and in the range 2.0–9.05 GPa [22]. Less relevant sources report 3.72 [6], 2.76 [23], 3.5 [8], and 2.9 GPa [24].

The elastic properties assigned to the RUC components are summarized in Table 1. The material input data and geometries are based on experiments carried out at the University of Michigan [1,22].

2.2. Mesoscale

The RUC geometry on the mesoscale needs to be fully described. The RUC is composed of axial fiber tows, bias (or braider) fiber tows inclined at a certain angle ϕ, pure matrix tows and connecting truss (or bar) elements; see Figs. 2, 3 and 4 (and for a justification of the use of truss elements, see Section 2.3). In Fig. 3, a plan view of half the RUC is provided to show the layout of the truss elements (an isometric or oblique view would be useless because of an extremely small gap between the axial and bias tows). The colors of tows were also changed so the layout of the truss elements could be seen more clearly. Due to textile design, all the tows are undulated. For the RUC to be periodically repetitive, the RUC must accommodate one full wave of the undulation, which may be idealized as approximately sinusoidal. The pure matrix tows represent the matrix (polymeric resin) between the axial tows. The truss elements approximate the connections between the axial and bias tows, provided by the matrix at the peaks and valleys of the bias tow undulations. The size of the RUC for each bias tow angle is shown in Fig. 2.

The axial and inclined bias tows terminate with cross sections that are orthogonal to the fiber direction, which makes it possible to capture the fact that, within the tows, the cracks form in either normal or parallel planes, but not in planes inclined to the fiber direction. As a result, the RUC has non-smooth boundaries with protrusions and indentations. In spite of that, the RUC is periodically repetitive in axial, lateral and out-of-plane directions.

Fig. 4 presents a typical RUC with the bias tow angle of $\phi = 30°$. The figure further shows, from left to right, the biased fiber tows, the biased and axial fiber tows, and the tows with pure matrix pockets. Although the actual cross sections of the tows are lenticular of varying distortions, needed to accommodate the tow crossings, for the sake of simplicity they are assumed to be rectangular with a constant aspect ratio while preserving the correct cross sectional area. For this reason, the tow geometry implies some inter-penetrations as well as some open spaces. However, this does not matter from the mechanics viewpoint, since the tow volume, stiffness and centerline geometry are preserved.

The bias tows are firmly connected by the polymer resin to the axial tows at the peaks and valleys of the bias tow undulations. The connections resist out-of-plane forces (including those from tow buckling), in-plane shear deformations and

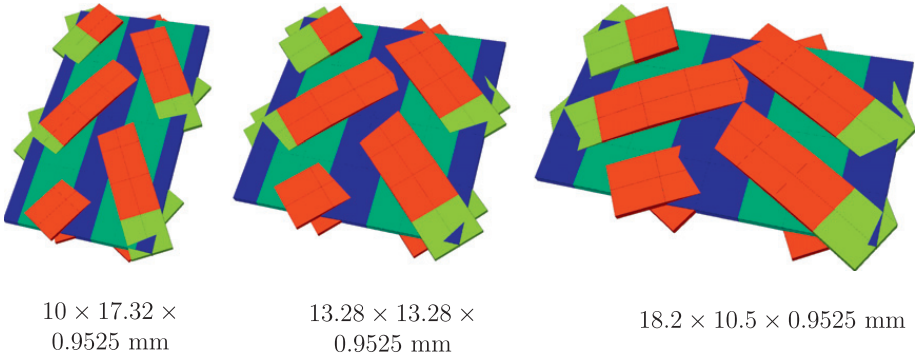

Fig. 2. RUCs with bias tow angles of 30° , 45° and 60° and their dimensions.

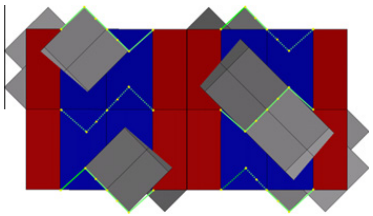

Fig. 3. Plan view of the layout of truss elements in half the RUC.

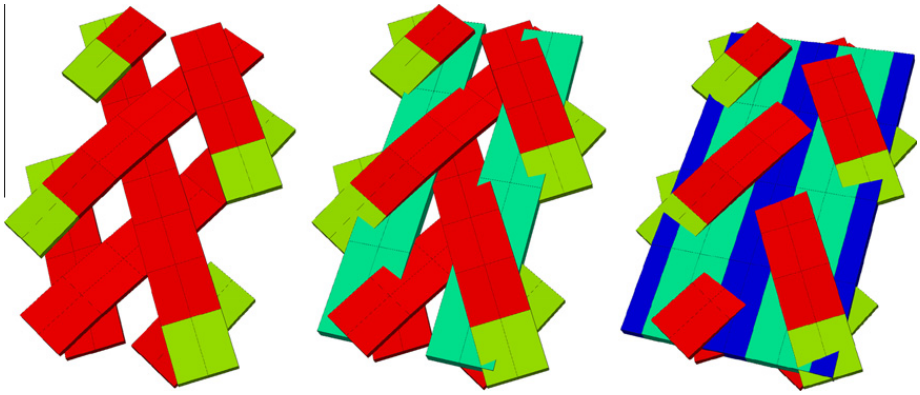

Fig. 4. Decomposition of RUC into bias and axial tows and assembled RUC with connectors. The bias tow angle corresponds to 30°.

in-plane tow rotations caused by loads. For simplicity, each of these connections is represented by a collection of truss elements (or bars) which connect specific nodes on the axial tows to nodes on the contacting bias tows (see also Section 2.3). Each truss element is assumed to behave as an elastic-damaging spring. The cross-sectional area of the truss elements (bars) can be arbitrarily chosen since their elastic stiffness and strength are the subject of calibration. Although the truss element stiffness must be calibrated empirically, the same stiffness may be used for various bias tow angles and undulation amplitudes.

The fact that here the tow cross sections and the pure matrix are not subdivided into many finite elements greatly reduces the computational burden while still capturing the essential physical behavior. Each RUC contains 987 nodes with 2961 degrees of freedom, 96 20-node quadratic brick elements and 166 truss elements (or bars). The rectangular dimensions of the tows are given in Table 2.

2.3. Should not the matrix between the tows be subdivided into many finite elements?

Many researchers would be tempted to answer yes. However, for softening damage and fracture, such a subdivision is normally counterproductive.

A subdivision of the pure matrix between the tows into many finite elements would lead to difficult, yet unresolved, problems in the modeling of softening damage and fracture, in which the material characteristic length of the subdivided matrix, defining the fracture behavior, must be known. The main problem is that there is no way to determine this length

Table 2
Tow sizes for RUC geometry.

Property	Values		
Bias tow angle (°)	30°	45°	60°
Axial tow width (mm)	2.940	3.704	4.564
Axial tow height (mm)	0.532	0.381	0.399
Bias tow width (mm)	2.630	2.995	3.022
Bias tow height (mm)	0.284	0.230	0.310
Axial tow spacing (mm)	5.00	6.64	9.10

computationally. It would have to be arbitrarily assumed, which could fit some test data but not others (in detail, see [13]), and would negate the purpose of multiscale analysis. Even if this length were guessed correctly, one would have to implement for the matrix between the adjacent tows some suitable type of nonlocal model serving as a localization limiter [13]. This would lead to complex programming.

Without introducing a nonlocal or crack band model with a material characteristic length, the computer simulations would exhibit spurious mesh sensitivity to the element size in the matrix, i.e., different results would be obtained for different element sizes [13]. For an infinite mesh refinement in the pure matrix, such analysis would converge to a solution in which the fracture energy dissipation in the pure matrix is zero; see Ref. 12, chapters 7 and 8 for details.

Another problem is that if the pure matrix is subdivided into many elements, the propagation of multiple localized three-dimensional fracture surfaces through the pure matrix needs to be simulated. This brings about a host of further complexities if the modeling should be kept objective. If they are not overcome, the objectivity is again lost.

The use of truss (or connector) elements, which characterize damage and fracture energy dissipation on the mesoscale globally, is not only simpler but avoids all these problems.

2.4. Macroscale

The dimensions of the beams, tested at the University of Michigan [1], are given in Table 3 where L' is the distance between the supports. The geometry and typical loading configuration are seen in Fig. 5. The span-depth ratio of the beams is 2.583 and the ratio of notch depth to beam depth is $\alpha = 1/6$. A coarse mesh is used to capture the global behavior of the beams. The actual specimens used in the experiments consist of 8 plies having the total thickness of 7.62 mm. The simulations consider only one ply since, under in-plane loading, all the plies must behave identically. However, for a general loading, simulating only one ply would, of course, be insufficient.

A collection of RUCs is embedded above the notch and is constrained to the surrounding continuum elements. To reduce the computational demand, only the smallest number of RUCs needed to capture the observed failure mode is used. The continuum finite elements lying above the zone of embedded RUCs are also endowed with fracturing parameters; see Fig. 5. These continuum elements have no effect on the peak load but make the post-peak response drop steeply to a negligible residual stress. The drop is followed by elastic re-hardening. Assigning to these continuum elements a finite tensile strength in the lateral (horizontal) direction ensures that the crack could propagate further, after the zone of RUCs has been fractured. The strength of these elements is prescribed to be 20% greater than the flexural strength (or modulus of rupture), as determined empirically. The elevated strength limit ensures that the RUCs undergo damage before the beam elements would. Sensitivity analysis showed that by increasing the strength between 10% and 40% had a negligible effect on the peak load and a miniscule effect on the residual stress.

To determine the smallest, yet still sufficient, number of embedded RUCs required to obtain a realistic peak load and initial post-peak response, another series of tests is simulated. A notched beam, which is geometrically similar to those shown in Table 3, is generated with a length of 322 mm and height 125 mm. One, three and five RUCs with a 30° bias angle are then embedded above the notch and the responses are compared with the assigned real properties described later as part of the validation.

Fig. 6 confirms that the beam with three embedded RUCs gives almost the same response as the beam with five embedded RUCs. This indicates that in this particular case only three RUCs may be sufficient to obtain the correct peak load.

Table 3
Beam sizes used in experiments and simulations.

	Length L' (mm)	Depth D (mm)	Notch depth a (mm)
Size 1	196.85	76.20	12.70
Size 2	393.70	152.40	25.40
Size 3	787.40	304.80	50.80

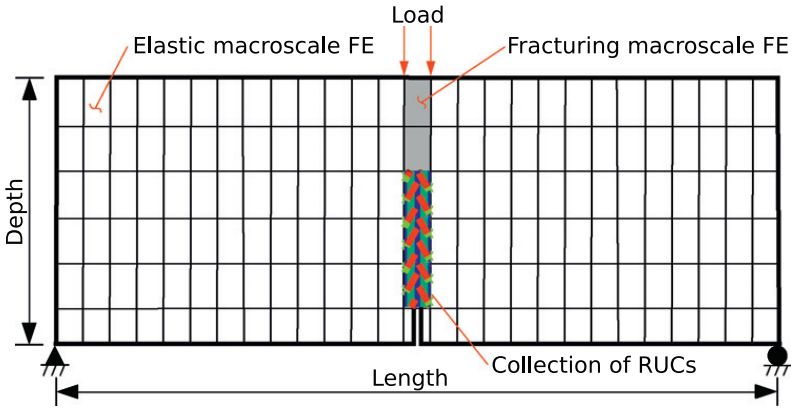

Fig. 5. Beam geometry with a notch and three embedded RUCs.

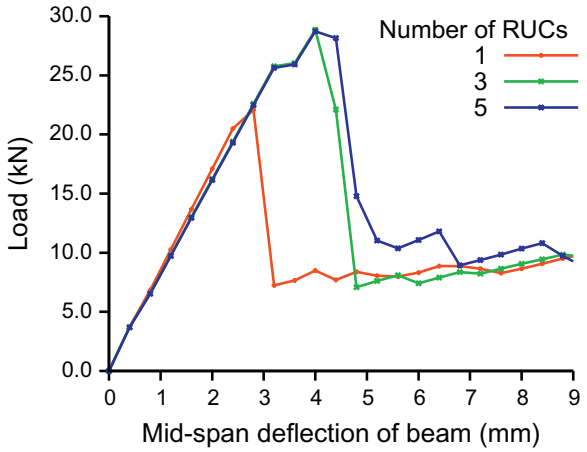

Fig. 6. Beam response with one, three and five embedded RUCs.

3. Finite element modeling

The FE analysis is based on a total stress–strain formulation, characterized by a secant stiffness matrix, $\boldsymbol{K}_i^S$. The solution leads to the matrix equation

$$\boldsymbol{K}_i^S \boldsymbol{r}_i = \boldsymbol{f}_i, \tag{8}$$

where $\boldsymbol{r}_i$ is a vector containing the total displacements at a load increment i, $\boldsymbol{f}_i$ represents a vector of total nodal forces and $\boldsymbol{K}_i^S$ contains the material properties and the geometrical information of the finite elements. Compared to an incremental formulation, the total formulation has the advantage of guaranteed convergence and a positive definiteness of the stiffness matrix, obviating any need for regularization schemes [25]. The assembly and solution of Eq. (8) is carried out in an open-source object-oriented finite element code called OOFEM (obtainable from www.oofem.org) [26].

The use of OOFEM was made necessary by the lack of availability of total stress–strain formulation in ABAQUS. This commercial code uses an incremental formulation for nonlinear problems, which creates a convenient framework for a hardening plastic material, for which there are no localization problems. On the other hand, incremental formulation generally runs into convergence problems for softening damage, for which the incremental stiffness matrix loses its positive definiteness and the Jacobian approaches zero. To overcome these problems, artificial numerical damping has been used [25]. However, this usually gives correct results within only one order of magnitude of strain rates, and adds various unnecessary complications which are automatically avoided by the total formulation. Commercial codes, such as ABAQUS, provide a general tool which might not be the best suited for a particular problem such as the present one.

Fig. 5 shows the typical geometry of a notched beam used in the analysis. To simplify the discretization of the system, two independent input files of RUC and beam are merged together using a python script. Master-slave nodes are then used to interconnect edges of adjacent RUCs boundaries. Hanging nodes are located on the continuum elements so that the edge of the RUCs can be attached. The mesh away from the expected cracking zone can be kept coarse and rather regular, while the mesh near the zone of potential cracking, consisting of the RUCs, is much more refined. All distal nodes of the beam are constrained against out-of-plane displacements.

3.1. Material law for damage with fixed crack orientation

The elastic behavior of the fiber tows is assumed to be transversely isotropic, and thus characterized by five independent elastic constants, E_{11}, E_{22}, ν_{12}, ν_{23} and G_{12}, see Table 1. Large macroscale elements outside of the cracking zone are also assumed to be transversely isotropic.

A simple and convenient modeling framework for introducing material degradation due to cracking damage is the continuum damage mechanics, proposed in 1958 by Kachanov [27]. However, to prevent spurious mesh sensitivity and capture the correct size effect [12,28], this classical theory must be suitably regularized by a characteristic length as a localization limiter, imposed by the element size within the RUC, which is proportional to the size of the RUC.

Since localized fracture breaks transverse isotropy, the continuum damage mechanics necessitates six independent internal damage variables d_p, with $p \in \{11, 22, 33, 23, 31, 12\}$, each of which ranges from 0 to 1. A fixed crack orientation is assumed, aligned with a local material coordinate system. Matrix notation of the compliance tensor $\boldsymbol{H}$ thus takes the form:

$$\boldsymbol{H} = \begin{bmatrix} \frac{1}{(1-d_{11})E_{11}} & -\frac{\nu_{21}}{E_{22}} & -\frac{\nu_{31}}{E_{33}} & 0 & 0 & 0 \\ -\frac{\nu_{12}}{E_{11}} & \frac{1}{(1-d_{22})E_{22}} & -\frac{\nu_{32}}{E_{33}} & 0 & 0 & 0 \\ -\frac{\nu_{13}}{E_{11}} & -\frac{\nu_{23}}{E_{22}} & \frac{1}{(1-d_{33})E_{33}} & 0 & 0 & 0 \\ 0 & 0 & 0 & \frac{1}{(1-d_{23})G_{23}} & 0 & 0 \\ 0 & 0 & 0 & 0 & \frac{1}{(1-d_{31})G_{31}} & 0 \\ 0 & 0 & 0 & 0 & 0 & \frac{1}{(1-d_{12})G_{12}} \end{bmatrix}. \tag{9}$$

The elastic constants of the matrix follow the well-known restrictions of isotropy, e.g. $G_{23} = E_{22}/2(1 + \nu_{23})$. The matrix of the material stiffness tensor, required for assembling the structural stiffness, is easily obtained by the inversion of $\boldsymbol{H}$. The constitutive law in the total stress–strain formulation has the form:

$$\boldsymbol{\varepsilon} = \boldsymbol{H}(d_{11}, d_{22}, \ldots, d_{12}) : \boldsymbol{\sigma}. \tag{10}$$

The damage criterion is based on the concept of strength (or ultimate stress), although more advanced criteria using a combination of stresses and strains exist [25,29].

Fig. 7 shows the stress–strain law used in all simulations. Linear softening is assumed because it gives an explicit formulation which requires no iterations, unlike exponential or bilinear softening [30]. Damage occurs when any of the six stress components exceeds the prescribed strength $f_{p,0}$, i.e.

$$|\sigma_p| \geqslant |f_{p,0}|. \tag{11}$$

The $f_{p,0}$ values for compression and tension can be different.

At the point of damage initiation, the characteristic element length l_p and $\varepsilon_{p,E}$, see Fig. 7, are known. l_p, which is the width of the softening zone within an element, is generally different for each failure mode or for elements of different sizes. To overcome the mesh dependence on $G_{f,p}$ and to ensure objectivity, the crack band model is used [31]. Given the fracture energy $G_{f,p}$, the maximum strain $\varepsilon_{p,0}$, reached when the stress is reduced to 0, is evaluated as follows:

$$\varepsilon_{p,0} = \varepsilon_{p,E} + \frac{2G_{f,p}}{f_{p,0} l_p}. \tag{12}$$

The properties of the pure matrix, including its fracture energy, are known from reference manuals but, except for one limited study [36], no usable data exist for the fiber tows (for which significantly different fracture energies were reported depending on the number of fibers in a tow). Thus, the fracture energy G_f of the tows and the tensile strength f_t were here

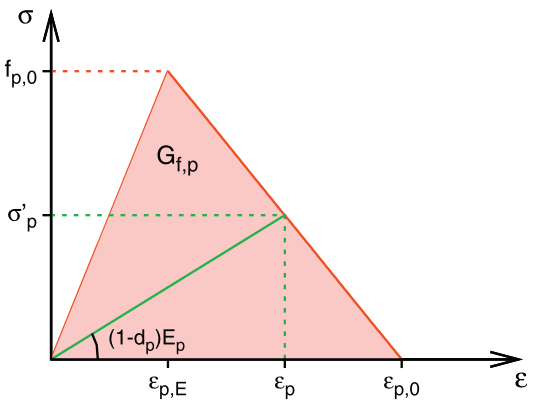

Fig. 7. Assumed linear softening law for each orthogonal direction.

determined by optimum fitting of the size effect test results, while the constituent properties known from manuals were used as the input. The G_f and f_t values obtained for one bias tow angle should, in principle, be usable for other tow angles but this could not be shown for the specimens provided since the fiber volume fractions for various tow angles differed. In this optimization it is necessary avoid snap-back instability which begins when the post-peak softening slope in the constitutive law Fig. 7 becomes vertical. This condition provides a useful minimum bound on the admissible G_f values, as given by Eq. (13) (this bound depends on Young's modulus as well as the characteristic element length, and since Young's modulus and the element size of the supplied specimens with different tow angles differ, the G_f values do, too).

When the finite element size in the crack band model is increased sufficiently, the post-peak stress strain relation switches from softening to snap-back, in order to maintain the specified fracture energy value. In computations, this leads to instability, lack of convergence and dynamic response. To ensure that no snap-back could occur in the effective stress–strain relation at some integration point, a certain minimum value of fracture energy $G_{f,p,min}$ must be imposed on each finite element (for explanation, see [12, p. 251] and also [38,11]. Since the characteristic element size l_p is roughly equal to the crack band width, one thus obtains:

$$G_{f,p} \geqslant G_{f,p,min} = \frac{f_{p,0}^2 l_p}{2E_p}. \tag{13}$$

where E_p = elastic modulus in the direction p.

The point of damage initiation could be identified exactly only in the ideal case of infinitely small load increments, which is unattainable. Hence, one needs to interpolate between the first equilibrated post-peak increment and the previously converged increment, so as to achieve a good approximation even when the loading steps are not very small.

The evolution of the damage parameters is based on the evolution of the corresponding strain, ε_p, and the maximum strain achieved thus far, $\kappa_p^{\pm}$;

$$\text{if} \begin{cases} \varepsilon_p > \kappa_p^- \wedge \varepsilon_p < \kappa_p^+ & \text{damage does not grow,} \\ \varepsilon_p \leqslant \kappa_p^- \vee \varepsilon_p \geqslant \kappa_p^+ & \text{damage may grow.} \end{cases} \tag{14}$$

When the damage can grow, the desired stress σ_p is evaluated from the actual strain ε_p and the known softening parameters

$$\sigma_p' = f_{p,0} \frac{\varepsilon_{p,0} - \varepsilon_p}{\varepsilon_{p,0} - \varepsilon_{p,E}}. \tag{15}$$

The damage variables d_p ensue from Eq. (9); for example

$$d_{11} = 1 - \frac{\sigma_{11}}{E_{11}\left(\varepsilon_{11} + \frac{\nu_{21}}{E_{22}}\sigma_{22} + \frac{\nu_{31}}{E_{33}}\sigma_{33}\right)}, \tag{16}$$

$$d_{12} = 1 - \frac{\sigma_{12}}{G_{12}\varepsilon_{12}}. \tag{17}$$

To meet the thermodynamic restrictions, no decrease of the damage parameter in permitted.

The constitutive law from Eq. (10) was verified by uniform stretching of one brick element in the y direction. Fig. 8 shows that the damage law works as expected in the tensile and compressive regions.

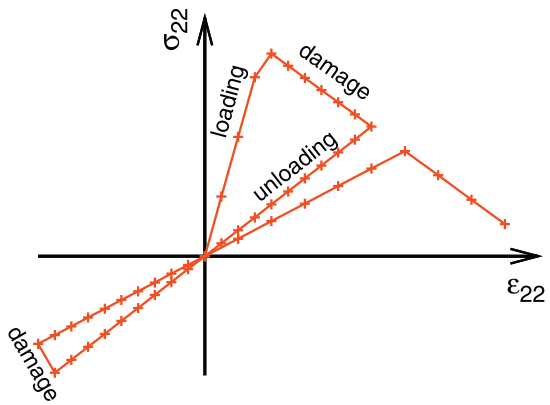

Fig. 8. Stress–strain response of a linear brick element stretched in the y direction.

4. Computations, results and discussion

4.1. Calibration of elastic response of RUC

The elastic properties of the tows and epoxy matrix used in the analysis are summarized in Table 1. The connections between the axial and bias tows (represented by truss elements, or bars) are characterized by their lengths, which are given by the tow geometry, and by their cross-section area A_c and Young's modulus E_c, both of which are assumed to be the same for all the truss elements. In the present quasi-static problem (i.e., a problem in which, by contrast to wave propagation, the inertial forces are negligible), only the product A_cE_c matters. The reason is that it alone determines the stiffness of the truss elements. It follows that either E_c or A_c may be chosen and the other then follows by elastic calibration. Here we chose $A_c = 1\ \text{mm}^2$, which makes the volume of all the connectors roughly equal to the volume of the pure matrix between the tows (although this equality is here unnecessary, as it would matter only for inertial forces in wave propagation). Therefore, the only connector characteristic that is identified by matching the overall elastic response of the RUC is Young's modulus E_c.

The elastic calibration depends on two effects: the boundary conditions, and the finite element (FE) size. Periodic boundary conditions are used since they generally are best for providing the overall elastic properties of the RUC, independent of specimens size or discretization [32]. Fig. 9 testifies to a fast convergence of E_{11} to the experimental value when the mesh is being refined (this is the so-called h-version of FE). The convergence validates the way the RUC has been constructed and assigned the elastic properties of the individual components. The mesh was then made coarser to not only improve computational efficiency, but also to better capture the fracturing within the fiber tows and the pure matrix pockets which are spaced laterally between the axial fiber tows. A finer mesh does improve accuracy for non-softening behavior, however, it inevitably leads to computational problems when simulating softening damage and fracture; see Section 2.3.

Mixed boundary conditions are more realistic when the RUC alone is compared with the performance of an embedded collection of RUCs. The boundary conditions imposed are based on the following considerations:

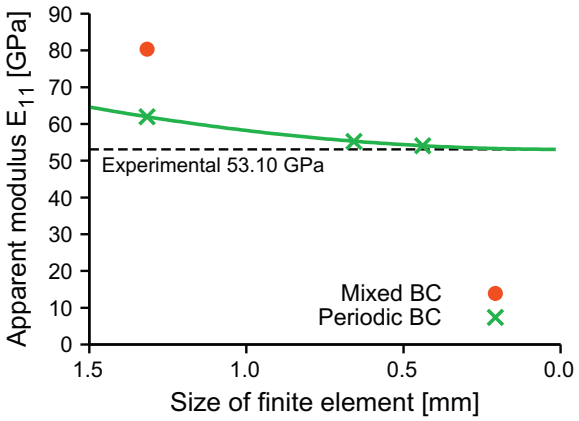

Fig. 9. Convergence of apparent modulus E_{11} with varying element size. Periodic or mixed boundary conditions are imposed. RUC with 30° bias tow angle.

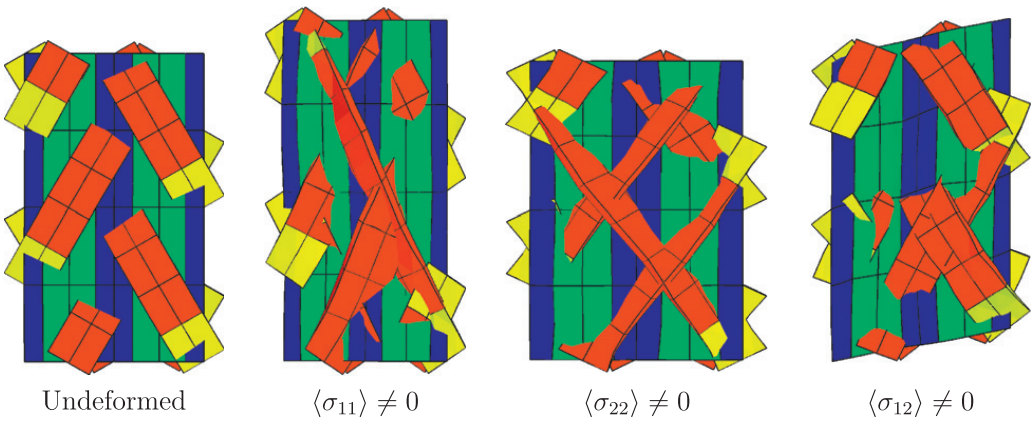

Fig. 10. Deformation of RUC under three deformation modes, bias tow angle 30°. Mixed boundary conditions apply.

1. In the analysis of three-point-bend specimens, the RUCs are embedded in the beam and their boundaries are kinematically attached to the neighboring macroscale finite elements. In this particular case, the kinematic boundary conditions are applied.
2. Equal nodal displacements are enforced at the border between two RUCs to ensure continuity of the axial and bias tows.

For these reasons, the elastic calibration over one RUC consists of kinematic uniform boundary conditions for the in-plane directions and of periodic boundary conditions for the out-of-plane direction; see Fig. 10. In planar problems, such as the quasi-static three point bending tests simulated in this study, it is acceptable to consider any out of plane deformation as periodic, since only one layer of an 8-ply composite is being simulated. The calibration resulted in truss (or bar) element moduli of 35.0 GPa, which is the optimal value assigned to all the trusses in all RUCs. This value is found to be virtually independent of the number of RUCs used in the calibration.

Table 4
Apparent homogenized elastic properties from one RUC with imposed mixed boundary conditions. Experimental values are in parentheses.

Bias tow angle	30°	45°	60°
E_{11} (GPa)	80.24 (53.10 ± 0.78)	36.97 (27.88 ± 1.15)	35.47 (23.17 ± 0.85)
E_{22} (GPa)	11.66 (7.29 ± 0.75)	13.88 (13.74 ± 1.17)	35.36 (22.09 ± 0.09)
G_{12} (GPa)	10.67	7.95	8.02
ν_{12} (–)	0.93 (0.93 ± 0.03)	0.61 (0.59 ± 0.06)	0.27 (0.30 ± 0.01)
ν_{21} (–)	0.12 (0.12 ± 0.02)	0.23 (0.32 ± 0.01)	0.30 (0.34 ± 0.02)

Table 5
Elastic response of RUC with a bias tow angle of 30° with varying truss element Young's modulus.

Truss elements Young's modulus (GPa)	E_{11} (GPa)	E_{22} (GPa)	ν_{12}	ν_{21}
15	80.17	11.60	0.93	0.124
35	80.24	11.66	0.93	0.124
55	80.26	11.61	0.92	0.124

Table 6
Elastic response of RUC with a bias tow angle of 60° with varying truss element Young's modulus.

Truss elements Young's modulus (GPa)	E_{11} (GPa)	E_{22} (GPa)	ν_{12}	ν_{21}
15	31.36	35.23	0.28	0.296
35	31.47	35.36	0.27	0.297
55	31.47	35.40	0.28	0.299

Table 7
Strength and fracture energies assigned to the RUC components. The indexes mean *t*-tension, *c*-compression, *s*-shear.

Bias tow angle		30°	45°	60°
Axial and bias tows	$f_{11,tc}$	±4950[a] MPa	±3700[a] MPa	±2550[a] MPa
	$G_{f,11,tc}$	63.5[e] N/mm	41.5[e] N/mm	19.7[e] N/mm
	$f_{22,33,t}$		80[b] MPa	
	$f_{22,33,c}$		−241[b] MPa	
	f_s		34.9[b] MPa	
	$G_{f,22,33,t}$		0.185[cb] N/mm	
	$G_{f,22,33,c}$		1.05[e] N/mm	
	$G_{f,s}$		0.485[db] N/mm	
Epoxy resin		f_t = 80 MPa [34], f^c = −241 MPa [34] f_s = 34.9 MPa [33] $G_{f,t}$ = 0.620[ce] N/mm, $G_{f,c}$ = 5.6[de] N/mm $G_{f,s}$ = 0.485 N/mm [35]		

[a] Reported tensile strength of carbon tows 3.8 and 4.5 GPa [7].
[b] Taken from the property of pure epoxy resin, indicated at the bottom of the Table.
[c] Reported 0.185 N/mm [35].
[d] Reported 0.485 N/mm [35].
[e] Assigned the minimum fracture energy which does not cause the snap-back, see Eq. (13).

Table 4 compares the RUC elastic performance to the experiments of Waas et al. [22]. Poisson's ratios are matched reasonably well for all the bias tow angles. All the apparent elastic moduli are up to 60% greater, because of mixed boundary conditions and a coarse RUC discretization.

An analysis was performed to evaluate the sensitivity of the elastic response of the RUC to different Young's moduli of truss elements. Table 5 summarizes the results for a bias tow angle of 30°, and Table 6 for a bias tow angle of 60°.

4.2. Strength and fracture energy of RUC components

Table 7 gives a summary of the strength and fracture energy values prescribed to all RUC components. The shear strength of the epoxy resin is assumed to be 34.9 MPa [33], although values as high as 60 MPa have been reported [34]. However, this discrepancy is no problem since the strength and fracture properties of the epoxy have a negligible effect on the peak loads of the beams. The fracture energies of the fiber tows, except for those for the fiber direction, are inherited from the epoxy resin. If necessary, they are raised to the minimum fracture energy value that suffices to avoid the snap-back; see Eq. (13).

The strength of the axial and bias tows had to be calibrated from experimental data. The simulations show that a dominant failure mechanism of the beams consists of a tensile failure of the bias tows, which is controlled by their tensile strength and fracture energy. The strength of the axial fiber tows can be chosen to be equal to the strength of the bias tows since they have a comparable volume fraction for each bias tow angle. Besides, the contribution of the axial tows to this type of failure is found to be negligible, which is not surprising since the stresses in the axial tows are several times lower than those in the bias tows.

The prescribed tensile strength of the bias tows ranges between 2.55 and 4.95 GPa, which appears to be quite reasonable. The tensile strength of a single carbon fiber was reported to be 4.96 GPa [9] and 5.8 GPa for a four-filament tow [36]. In the present case, the combined fiber volume fraction is between 0.54 and 0.77 [22]; see Table 1. The transversal strengths $f_{22,tc}$ and $f_{33,tc}$ of the fiber tows are expected to be governed by the strength of the epoxy matrix.

The damage initiation criterion from Eq. (11) is expressed in terms of stresses. To achieve nearly equilibrated stresses, equilibrium iterations are needed prior to applying this criterion. Fig. 11 shows that five iterations suffice, as determined by sensitivity analysis. These iterations, used in all computations, generally take less than 10% of the overall CPU time.

4.3. Simulations of fracture of notched beams

Fig. 12 compares the simulated load–deflection curves and experimental peak loads. Generally, a nearly linear response is observed before the peak load, after which quasi-brittle failure immediately follows. The residual strength in the simulated curves is caused by transverse and shear load-bearing capacity of the bias tows.

Fig. 13 displays the best of the three experimental results for each bias tow angle, and compares them to the simulated results (dashed line). The smallest test specimens are seen to exhibit the most ductile response, which is typical of quasibrittle size effect.

Fig. 14 shows the macroscale layout and deformations for the smallest beam with the bias tow angle of 30°. The subplots on the left and right show the beam at, and just after, the peak load. The deformation is magnified three-times.

The damage mechanism can be discerned in more detail in Fig. 15. It consists of the bridging of cracks by the fiber tows, and is similar for all tow angles and beam sizes. According to the present simulations, the cracking of matrix and fibers proceeds in the following sequence:

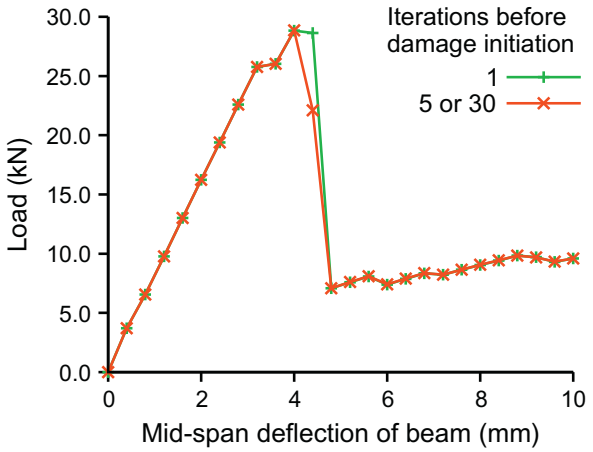

Fig. 11. The role of iterations on the introduction of damage.

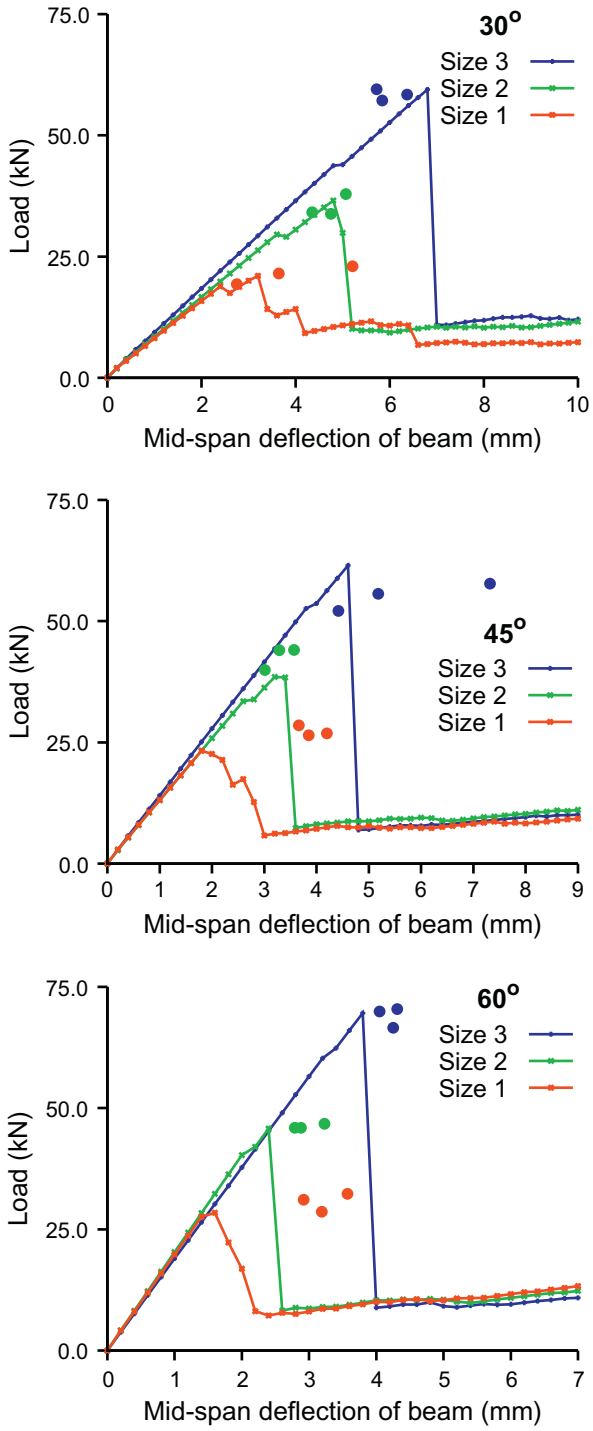

Fig. 12. Load–deflection plots for 30° , 45° and 60°. The solid circles represent peak loads from experiments.

1. A crack initiates in the matrix shortly after the application of load. The beam stiffness drops by up to 15%, which is manifested through a change of slope, as can be noticed in Fig. 12. The early damage of the epoxy matrix is consistent with a previous report [24].
2. At 50% of the peak load, shear damage occurs in the bias tows near the connection points of the truss elements. A minor shear damage may also occur in the axial tows, however only a negligible reduction in beam stiffness is noticed.
3. Shortly before the peak load, a few bias tows may fail in tension. This is what produces the discontinuous 'jumps' in Fig. 12.
4. At the peak load, typically two RUCs show a significant damage indicating formation of the fracture process zone.
5. The state at the first post-peak point shows intense tensile fracturing in several bias tows, but some stress is still transmitted through the undamaged bias tows.

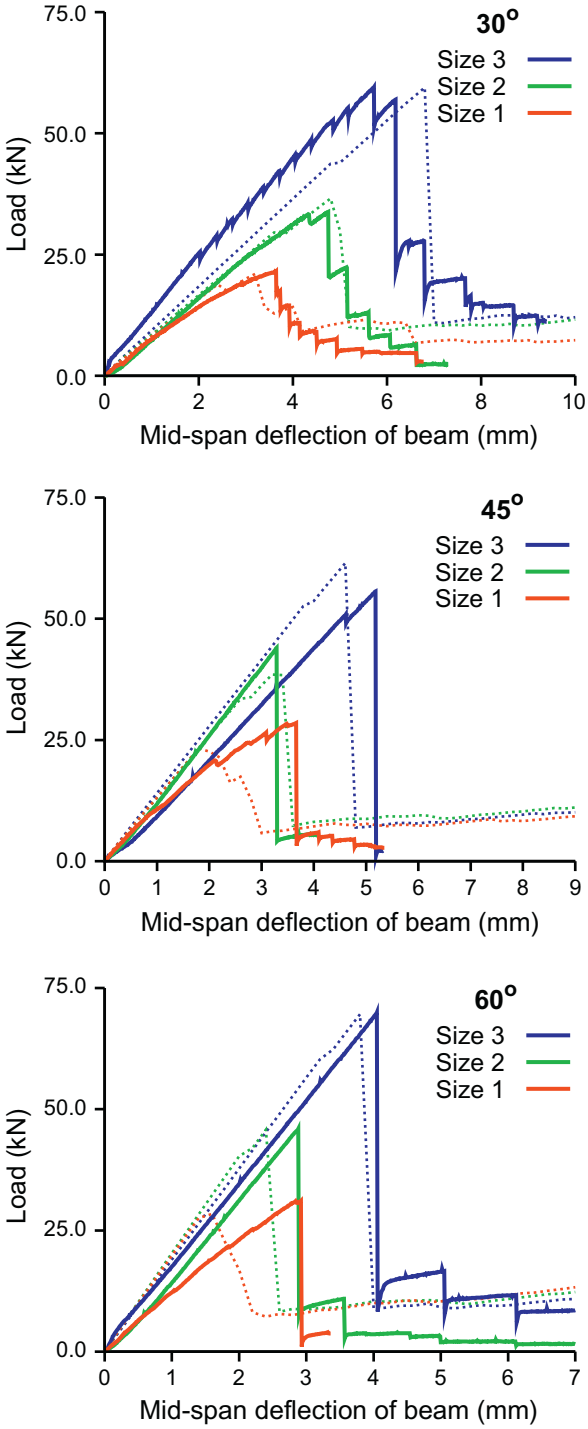

Fig. 13. Best fit with experimental data. The solid line represents the response from experiments, and the dotted line is the FE result.

A similar damage mechanism was described in [24,37]. A failed test specimen is shown in Fig. 16. It clearly demonstrates tensile failure of the bias tows obtained numerically.

Table 8 gives an overview of the details of computations on a single 32-bit CPU (3.2 GHz). The relative tolerance of 0.001 is prescribed for both the mid-span displacement and force equilibrium. Fifty load increments are executed in all the simulations, which are controlled by specified increments of the mid-span deflection. The factorization of the sparse stiffness matrix takes the majority of computational time. Typically 10–30 iterations are used during one load increment.

This may rise to 70 during significant damage, especially for the smallest beam sizes. The complete solution for all the sizes takes 14–16 h.

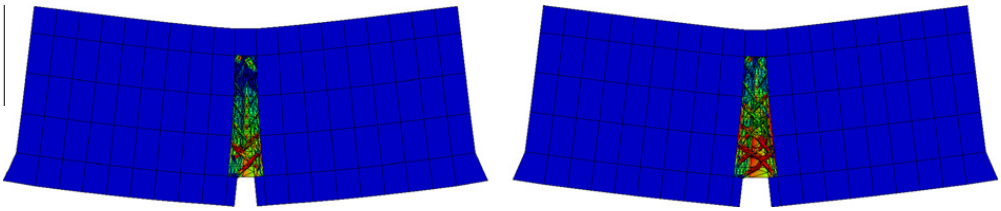

Fig. 14. The smallest beam "size 1", bias tow angle 30°. Left: the beam at the peak load, right: one step after the peak load. Colors (or shades) represent damage, the deformation is scaled 3×. (For interpretation of the references to color in this figure legend, the reader is referred to the web version of this article.)

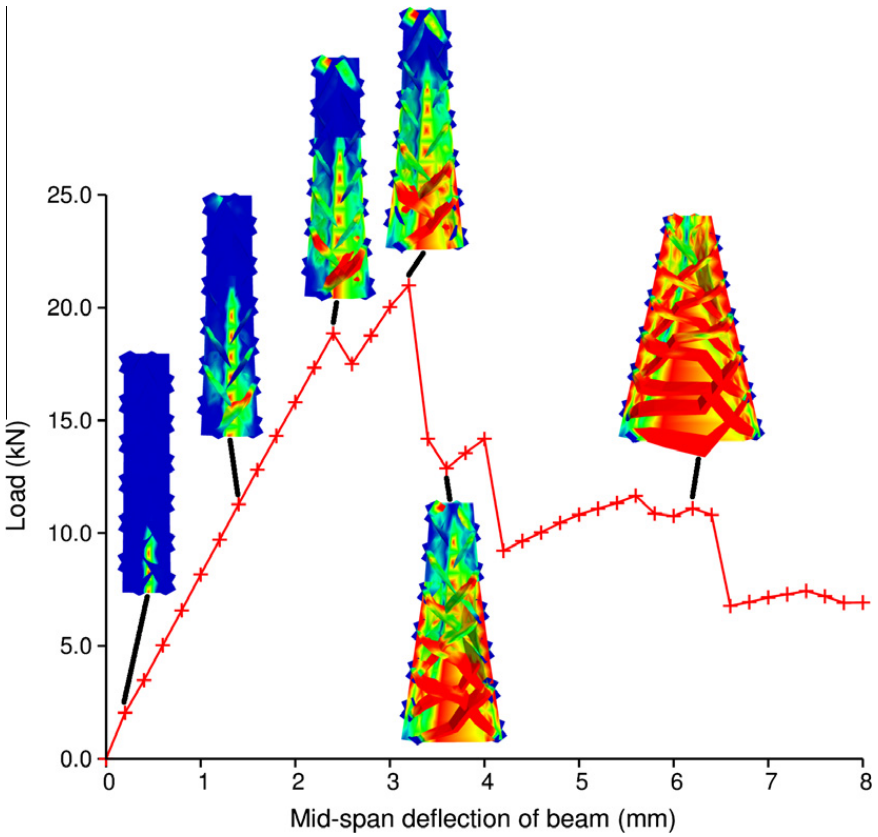

Fig. 15. Deformed shape of three embedded RUCs in the size-1 beam, bias tow angle 30° . Colors represent damage magnitude, the deformation scaled 3×. (For interpretation of the references to color in this figure legend, the reader is referred to the web version of this article.)

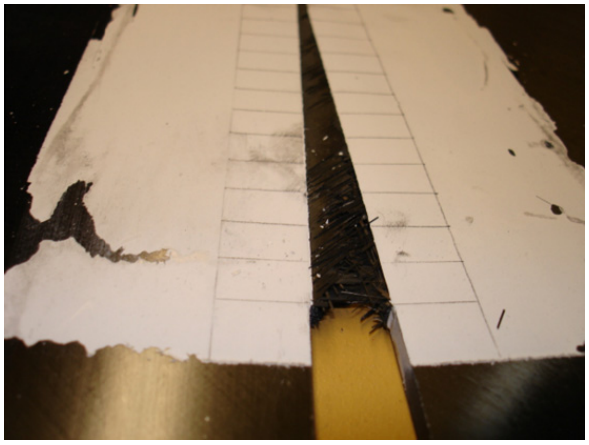

Fig. 16. A typical crack pattern observed in the experiments.

Table 8
Computational details.

Size	Size 1	Size 2	Size 3
Elements	591	887	1920
DoFs	7041	8007	11245
RAM (MB)	105	122	196
Factorization (s)	51	88	185
Elapsed real solution time (h)	14.23	14.45	16.38

4.4. Size effect

Softening damage or fracture automatically gives rise to a non-statistical size effect [12,38–42]. This is the most important consequence of quasibrittle fracture, and is essential for correct and unambiguous identification of the material fracture properties.

In a very small specimen or structure, the fracturing zone (or fracture process zone, FPZ) extends, at maximum load, over nearly the entire cross section of the specimen. In very large specimens, the FPZ is almost negligible compared to the structure size. This is because the FPZ size, which is related to the material characteristic length (which in turn is roughly equal to the unit cell size), remains nearly constant as the structure size is increased. Thus the finite FPZ size causes quasibrittle behavior, i.e., a damage behavior that is transitional between nearly plastic (or ductile, quasi-plastic) behavior, typical of small structures, and brittle behavior, typical of large structures.

Ductile structures always loose their load carrying capacity at the same maximum stress, or at the same nominal stress value. In other words, there is no size effect. But in quasibrittle structures, the value of nominal stress σ_{Nu} at failure decreases with the structure size, D. For similar cracks in geometrically similar perfectly brittle structures, $\sigma_{Nu} \propto D^{-1/2}$ according to the linear elastic fracture mechanics (LEFM), which gives a straight line of slope $-1/2$ in the size effect plot of $\log \sigma_{Nu}$ versus $\log D$.

In quasibrittle structures, the size effect plot is a transition from a horizontal line for small sizes to the inclined asymptote of slope $-1/2$ for large sizes. This is important for the identification of cohesive fracture properties of the material.

All the structures with sizes not too small and not too large with respect to the characteristic size have a strength that scales approximately according to the size effect law

$$\sigma_{Nu} = \frac{Bf'_t}{\sqrt{1 + D/D_0}}, \tag{18}$$

where Bf'_t and the transitional structure size D_0 are unknown parameters. This law has been derived by asymptotic matching of the strength scaling for the perfectly ductile case at small sizes and the perfectly brittle case at large sizes.

The parameters of this law can be identified from tests of maximum load of geometrically similar specimens of different sizes, provided that a sufficiently broad size range is used. The same law is also observed in simulation results with the cohesive crack model, the crack band model and the nonlocal damage model [12]. Thus, the material parameters of the RUC can be identified by fitting the size effect simulations to the test data.

The simulated peak loads have been fitted by Eq. (18) using the Levenberg–Marquardt algorithm. Fig. 17 shows the size effect law for specimens with all the three bias tow angles. Angle 60° shows the most brittle behavior. In all the three graphs, the horizontal dashed line represents the strength for a very small size, which typically follows from plasticity analysis, and the negatively sloped line is the strength limit based on linear elastic fracture mechanics.

4.5. Determination of fracture energy and effective process zone length

The dimensionless energy release rate $g(\alpha)$ is equal to $k^2(\alpha)$, where $k(\alpha) = b\sqrt{D}K_I/P$ = dimensionless stress intensity factor; $\alpha = a/D$, a = crack length (including the notch), D = specimen dimension (or depth), K_I = mode I stress intensity factor, P = load and b = specimen width. Graphs or tables of K_I as a function of α exist for many specimen geometries, but only for isotropic materials [43]. The 2DTBC is orthotropic, and so it is necessary to determine $k(\alpha)$ numerically (e.g. [44]).

The fracture parameters can be determined from size effect tests, as shown in [11,12,41,45,46]. The nominal strength σ_N is defined as

$$\sigma_N = c_N \frac{P}{bD}, \tag{19}$$

where P is the maximum load, c_N is a constant chosen for convenience, and b and D are the specimen thickness and depth, respectively. Eq. (18) for the size effect law may be rewritten in terms of the LEFM functions [12,45,46]:

$$\sigma_N = c_N \left(\frac{EG_f}{g'(\alpha_0)c_f + Dg(\alpha_0)} \right)^{1/2}. \tag{20}$$

Here G_f is the fracture energy of the material, c_f is the effective length of the FPZ (equal to about one half of the actual FPZ length for an infinitely large specimen), $\alpha_0 = a_0/D$, where a_0 is the length of the notch.

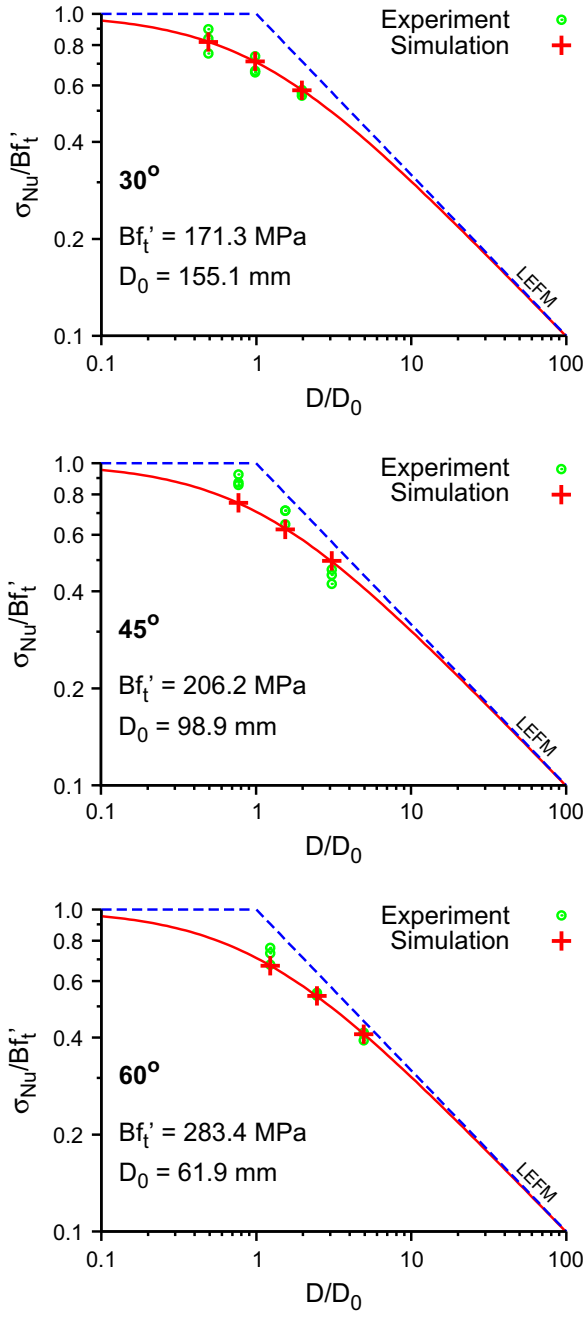

Fig. 17. Fitting of size effect law for beams manufactured from 2DTBC, 30° , 45° and 60° bias tow angles.

A planar three-point-bend specimen, whose dimensions are normalized with respect to the specimen depth, is generated for each bias tow angle considered. A unit load is chosen for all the simulations.

To determine function $g(\alpha)$, the J-integral values, which are equal to the energy release rates $\mathscr{G}(\alpha)$, have been calculated numerically for several α values by ABAQUS. Then

$$g(\alpha) = \frac{E\mathscr{G}(\alpha)}{\sigma_n^2 D}, \tag{21}$$

where $\sigma_n = P/bD$ = nominal stress, analogous to Eq. (19) except that here P is the applied load, and generally not the peak load.

Since the global elastic response of the specimens has been determined from experiments, all the in-plane elastic constants were first normalized by E_{11}, and then used in the elastic material law of ABAQUS. The relative crack length is then varied from $\alpha = 0.14$ to $\alpha = 0.5$ and a fourth-order polynomial is fitted to the data. σ_N can then be calculated from Eq. (19). Since all the elastic constants in the material law are normalized with respect to E_{11}, and all the dimensions are normalized with respect to D, Eq. (21) reduces to $\mathscr{G} = g(\alpha)$.

Table 9
Fracture properties of composites for each bias tow angle.

	$\phi = 30°$	$\phi = 45°$	$\phi = 60°$
G_f (N/mm)	464.05	281.65	212.25
c_f (mm)	31.73	21.47	13.39

In view of Eqs. (18) and (20), the fracture energy G_f and the effective length of the fracture process zone c_f may now be calculated as

$$G_f = \frac{(Bf_u)^2}{c_N^2 E} D_0 g(\alpha_0), \tag{22}$$

$$c_f = \frac{g(\alpha_0)}{g'(\alpha_0)} D_0, \tag{23}$$

where Bf_u and D_0 are obtained by fitting the measured σ_N-values with the Levenberg–Marquardt optimization algorithm, and $c_N = 1.5$ length/depth. The resulting fracture energy, G_f, and the effective length of the process zone, c_f, are displayed in Table 9.

5. Conclusions

1. The multiscale finite element simulation of notched 2DTBC beams, in which the region of expected fracturing is replaced by a system of repetitive unit cells (RUCs), has proven to be capable of capturing the elastic response as well as the peak loads obtained experimentally by fracture tests of notched specimens of different sizes. The damage process identified by the analysis has also been shown to be realistic.
2. Both the simulation results and the tests clearly show a strong size effect, which is missed by computations that do not use fracture mechanics or nonlocal damage mechanics, and thus are not objective due to the non-inclusion of a material characteristic length scale.
3. The analysis of the size effect tests requires the energy release rate function to be determined for the macroscopic orthotropic elastic properties of the composite. This can be easily accomplished using finite element software, such as ABAQUS. The fracture energy G_f and the effective process zone size c_f readily follow.
4. The present approach can capture the effects of different volume fractions of resin and tows, different inclinations of braider tows and different properties of the fibers and resin.
5. For structures with crack locations unknown *a priori*, the present analysis would be (without an adaptivity extension) computationally very intensive. Nevertheless, the present RUC approach is valuable for calibrating a more computationally efficient approach, such as the microplane model [21], when the full range of experiments is not available.

Acknowledgements

This research was supported by the Automotive Composites Consortium (ACC) under a United States Automotive Materials Partnership (USAMP) Cooperative Agreement No. DE-FC05-95OR22363 with the U.S. Department of Energy (US-DoE). The authors are grateful for the support and monitoring of the Predictive Technology Development and Crash Energy Management Group (ACC100) of the ACC. The authors acknowledge that this research was funded, in whole or in part, by the US-DoE, and such support does not constitute an endorsement by the US-DoE of the views expressed herein. Additional partial funding for V. Smilauer's visit to Northwestern University, provided by GACR 103/08/1639 (Czech Republic), is also acknowledged. Finally, thanks are due to Prof. Bořek Patzák, the creator of OOFEM at the Czech Technical University in Prague, for helpful comments on implementation.

References

[1] Bažant ZP, Waas AM, Hoover CG, Caner FC, Šmilauer V, Salvi A. Experimental characterization of size effects for 2DTBC specimens using RILEM standard test configuration. ACC progress report, Northwestern University and University of Michigan; 2009.
[2] Carvelli V, Poggi C. A homogenization procedure for the numerical analysis of woven fabric composites. Composites Part A 2001;32:1425–32.
[3] Nicoletto G, Anzelotti G, Riva E. Mesoscopic strain fields in woven composites: experiments vs. finite element modeling. Optics Lasers Engng 2009;4:352–9.
[4] Song S, Waas AM, Shahwan KW, Xiao X, Faruque O. Braided textile composites under compressive loads: modeling the response, strength and degradation. Compos Sci Technol 2007;67:3059–70.
[5] Waas AM, Schultheisz CR. Compressive failure of composites: part II – experimental studies. Prog Aerosp Sci 1996;32(1):43–78.
[6] Quek SC, Waas AM, Shahwan KW, Agaram V. Compressive response and failure of braided textile composites: part 1 – experiments. Int J Non-Linear Mech 2004;39(4):635–48. doi:10.1016/S0020-7462(03)00018-0.
[7] Quek SC, Waas A, Shahwan KW, Agaram V. Compressive response and failure of braided textile composites: part 2 – computations. Int J Non-Linear Mech 2004;39(4):649–63. doi:10.1016/S0020-7462(03)00019-2.
[8] Zeng T, Fang D, Lu T. Dynamic crashing and impact energy absorption of 3D braided composite tubes. Mater Lett 2005;59:1491–6.

[9] Huang J, Wang X. Numerical and experimental investigations on the axial crushing response of composite tubes. Compos Struct 2009;91(2):222–8.
[10] Hettich T, Hund A, Ramm E. Modeling of failure in composites by X-FEM and level sets within a multiscale framework. Comput Methods Appl Mech Engng 2009;197:414–24.
[11] Bažant ZP, Cedolin L. Stability of Structures: elastic, inelastic, fracture and damage theories. 1st ed. New York: Oxford University Press; 1991 [and 3rd ed., World Scientific Publishing, Singapore–New Jersey–London; 2010 (sec. 13.2)].
[12] Bažant ZP, Planas J. Fracture and size effect in concrete and other quasibrittle materials. CRC Press; 1998.
[13] Bažant ZP. Can multiscale–multiphysics methods predict softening damage and structural failure? Int J Multiscale Comput Engng 2010;8(1):61–7 [authorized republication from newsletter Mechanics, American Academy of Mechanics, 2007;36(5–6):5–12].
[14] Fish J, Shek K. Multiscale analysis of composite materials and structures. Compos Sci Technol 2000;60(12–13):2547–56. doi:10.1016/S0266-3538(00)00048-8.
[15] Kouznetsova V, Geers MGD, Brekelmans WAM. Multi-scale constitutive modelling of heterogeneous materials with a gradient-enhanced computational homogenization scheme. Int J Numer Methods Engng 2002;54(8):1235–60.
[16] Raghavan P, Ghosh S. Concurrent multi-scale analysis of elastic composites by a multi-level computational model. Comput Methods Appl Mech Engng 2004;193(6–8):497–538. doi:10.1016/j.cma.2003.10.007.
[17] Ghosh S, Bai J, Raghavan P. Concurrent multi-level model for damage evolution in microstructurally debonding composites. Mech Mater 2007;39(3):241–66. doi:10.1016/j.mechmat.2006.05.004.
[18] Song J-H, Belytschko T. Multiscale aggregating discontinuities method for micro–macro failure of composites. Compos Part B: Engng 2009;40(6):417–26. doi:10.1016/j.compositesb.2009.01.007 [blast/impact on engineered (nano)composite materials].
[19] Farhat C, Roux F-X. A method of finite element tearing and interconnecting and its parallel solution algorithm. Int J Numer Methods Engng 1991;32:1205–27.
[20] Zohdi T, Wriggers P. A domain decomposition method for bodies with heterogeneous microstructure based on material regularization. Int J Solids Struct 1999;36(17):2507–25. doi:10.1016/S0020-7683(98)00124-3.
[21] Caner FC, Bažant ZP, Hoover CG, Waas AM, Shahwan KW. Microplane model for fracturing of triaxially braided fiber–polymer composites. Theoretical and applied mechanics report no. 09-10/ACCm, Northwestern University (2009). ASME Journal of Engineering Materials and Technology; in press.
[22] Waas AM, Salvi A, Theis G. Size Effects in 2D triaxially braided composites with varying bias tow angles, privately communicated manuscript, University of Michigan; 2008.
[23] Toledo MWE, Nallim LG, Luccioni BM. A micro–macromechanical approach for composite laminates. Mech Mater 2008;40:885–906.
[24] Bahei-El-Din YA, Rajendran AM, Zikry MA. A micromechanical model for damage progression in woven composite systems. Int J Solids Struct 2004;41(9–10):2307–30. doi:10.1016/j.ijsolstr.2003.12.006.
[25] Lapczyk I, Hurtado JA. Progressive damage modeling in fiber-reinforced materials. Composites Part A 2007;38:2333–41.
[26] Patzák B, Bittnar Z. Design of object oriented finite element code. Adv Engng Softw 2001;32(10–11):759–67.
[27] Kachanov LM. On the time to failure under creep conditions. Izv AN SSSR Otd Tekhn Nauk 1958;8:26–31.
[28] Bažant ZP, Jirásek M. Nonlocal integral formulations of plasticity and damage: survey of progress. ASCE J Engng Mech 2002;128(11):1119–49.
[29] Hashin Z. Failure criteria for unidirectional fiber composites. Compos Struct 1980;32:255–64.
[30] Ožbolt J, Ananiev S. Scalar damage model for concrete without explicit evolution law. In: Bicanic HMN, De Borst R, Meschke G, editors. EURO-C 2003 computational modelling of concrete structures. A.A. Balkema; 2003. p. 287–94.
[31] Bažant ZP, Oh BH. Crack band theory for fracture of concrete. Mater Struct 1983;16:155–77.
[32] Kanit T, Forest S, Galliet I, Mounoury V, Jeulin D. Determination of the size of the representative volume element for random composites: statistical and numerical approach. Int J Solids Struct 2003;40:3647–79.
[33] Miwa M, Takeno A, Yamaguchi K, Watanabe A. Relation between shear strength at the fibre–matrix interphase and shear properties of resin matrix. J Mater Sci 1995;30:2097–100.
[34] Guo-dong F, Liang Jun WB-l. Progressive damage and nonlinear analysis of 3D four-directional braided composites under unidirectional tension. Compos Struct 2009;89:126–33.
[35] Haller P, Putzger R. Fracture energy in mode I and mode II of textile reinforced wood. In: Gdoutos E, editor. Fracture of nano and engineering materials and structures, proceedings of the 16th European conference of fracture. Netherlands: Springer; 2006. p. 453–4.
[36] Kumari S, Nithya S, Padmavathi N, Prasad NE, Subrahmanyam J. Tensile properties and fracture behaviour of carbon fibre filament materials. J Mater Sci 2009;45(1):192–200.
[37] Prasad NE, Kumari S, Kamat SV, Vijayakumar M, Malakondaiah G. Fracture behaviour of 2d-weaved, silica–silica continuous fibre-reinforced, ceramic–matrix composites (cfccs). Engng Fract Mech 2004;71(18):2589–605.
[38] Bažant ZP. Size effect in blunt fracture: concrete, rock, metal. ASCE J Engng Mech 1984;110(4):518–35.
[39] Bažant ZP. Scaling of quasibrittle fracture: asymptotic analysis. Int J Fract 1997;83(1):19–40.
[40] Bažant ZP, Chen E-P. Scaling of structural failure. Appl Mech Rev ASME 1997;50(10):593–627.
[41] Bažant ZP. Scaling of structural strength. Massachusetts: Elsevier Butterworth-Heinemann; 2005.
[42] Bažant ZP. Scaling theory for quasibrittle structural failure. Nat Acad Sci 2004;101(37):13400–7.
[43] Tada H, Paris PC, Irwin GR. The stress analysis of cracks handbook. 2nd ed. MO: Paris Productions Inc.; 1985.
[44] Bao G, Ho S, Suo Z, Fan B. The role of material orthotropy in fracture specimens for composites. Int J Solid Struct 1992;29(9):1105–16.
[45] Bažant ZP, Kazemi MT. Determination of fracture energy, process zone length and brittleness number from size effect, with application to rock and concrete. Int J Fract 1990;44:111–31.
[46] Bažant ZP, Kazemi MT. Size effect in fracture of ceramics and its use to determine the fracture energy and effective process zone length. J Am Ceram Soc 1990;73(7):1841–53.